

Suppression of shear ionic motions in bismuth by coupling with large-amplitude internal displacement

Kunie Ishioka^{1,*} and Oleg V. Misochko²

¹*National Institute for Materials Science, Tsukuba 305-0047, Japan*

²*Institute of Solid State Physics, Russian Academy of Sciences, 142432 Chernogolovka, Moscow Region, Russia*



(Received 19 March 2024; revised 29 July 2024; accepted 30 August 2024; published 20 September 2024)

Bismuth, with its rhombohedral crystalline structure and two Raman active phonon modes corresponding to the internal displacement (A_{1g}) and shear (E_g) ionic motions, offers an ideal target for the investigation of the nonequilibrium phonon-phonon and electron-phonon couplings. We investigate the E_g phonon dynamics under intense photoexcitation by performing anisotropic transient reflectivity (TR) measurements on a 1-mm-thick bismuth single crystal at 11 K. The amplitude of the coherent E_g phonon is found to increase with incident pump fluence up to 10 mJ/cm² and then turns to an apparent decrease. This behavior is in stark contrast to the amplitude of the A_{1g} phonon in standard TR measurements, which increases monotonically up to 20 mJ/cm² and then saturates. The contrasting behaviors of the two phonon modes can be interpreted in terms of the strong coupling of the E_g oscillation with large-amplitude A_{1g} displacement in a highly excited electronic state, where dynamic fluctuation of the vibrational potential will lead to a quick loss in the E_g vibrational coherence. Unlike previous studies on thin Bi films on substrates we observe no sign of a transition to a high-symmetry phase and instead observe signs of partial damage of the crystalline surface at 28 mJ/cm², possibly due to less efficient cooling at the surface of the bulk crystal.

DOI: [10.1103/PhysRevB.110.094313](https://doi.org/10.1103/PhysRevB.110.094313)

I. INTRODUCTION

Bismuth has recently attracted renewed attention because of its surface accommodating topological insulating electronic states. As for the bulk Bi electronic states, it has been established that Bi is a semimetal with its Fermi surface consisting of three electron pockets at the L points of the Brillouin zone and one hole pocket at the T point [1], although their topological classification is still under debate [2–6]. The crystalline structure of Bi crystal is rhombohedral with $A7$ symmetry, as illustrated in Fig. 1(a), with the ground-state internal displacement along the trigonal (z) axis $u \equiv c_1/2(c_1 + c_2) = 0.2357$ and the trigonal shear angle $\theta_{A7} = 57.23^\circ$ [3,7,8]. This structure will be transformed to a simple cubic structure by a slight deformation to $u = 0.25$ and $\theta_{A7} = 60^\circ$ [1,9]. Theoretical simulations predicted that the electronic band structure of Bi could undergo phase transitions from a semimetal to a semiconductor and to a metal by tweaking u and/or θ_{A7} [1,3,7,8]. Correspondingly, a pressure-induced semimetal-semiconductor phase transition of Bi was reported experimentally [10,11].

The rhombohedral Bi crystal features two Raman active modes with A_{1g} and E_g symmetries, which are associated with the variations in u and θ_{A7} , respectively, as shown in Fig. 1(a). It has been theoretically demonstrated that the introduction of photocarriers [12,13] transforms the potential energy surface (PES) along the A_{1g} coordinate from a double well into a flattened single well, as schematically shown in Fig. 1(b). The susceptibility of the PES to the electronic excitation leads to

a significant enhancement of coherent A_{1g} phonons via the displacive excitation of coherent phonons (DECP) mechanism [14,15] and thereby makes the A_{1g} mode a model target for optical studies on nonequilibrium electron-phonon coupling [14,16–29]. In the DECP mechanism a photoinduced shift in the equilibrium coordinate gives a driving force that is dependent on excited carrier density N [15,30]. If the carriers are created sufficiently quickly and live sufficiently long (displacive limit), the coherent ionic displacement Q_z can be described by a shifted damped harmonic function:

$$Q_z(t) = Q_z^E - Q_z^0 \exp(-\Gamma_z t) \cos(2\pi \nu_z t), \quad (1)$$

with the initial amplitude defined by the equilibrium shift between the ground and excited states, $Q_z^0(N) \equiv Q_z^E(N) - Q_z^{\min}$. The DECP enhancement of the A_{1g} mode of Bi was experimentally confirmed by means of time-resolved x-ray diffraction (trXRD) [31–36] and was supported by density functional theory (DFT) calculations [12,13,32,37]. One of the interests of recent ultrafast spectroscopic experiments on Bi lies in the optical control of its structural and electronic phases. A single-shot transient reflectivity (TR) study on thin Bi films [38] observed the disappearance of the coherent A_{1g} oscillation signal under intense photoexcitation and attributed it to the theoretically predicted transition to a high-symmetry phase with a single-well PES. The threshold fluence for the phase transition was found to depend critically on the Bi film thickness, suggesting that the phase transition competes with the electronic transport in the depth direction on a subpicosecond timescale [26,39].

The E_g -symmetry mode of Bi has been much less explored by time-resolved experiments, despite the theoretical

*Contact author: ishioka.kunie@nims.go.jp

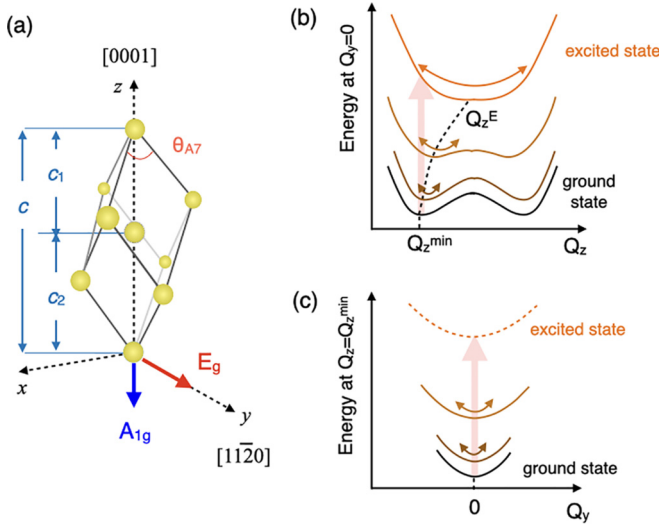


FIG. 1. (a) Crystalline structure of Bi together with the directions of the A_{1g} and E_g displacements. (b) and (c) Schematic illustrations of potential energy surfaces (PESs) along the (b) A_{1g} and (c) E_g coordinates for the ground and photoexcited states.

predictions that it could lead to a semimetal-semiconductor phase transition [1,3,7]. This is partly because of its much smaller amplitude compared to the A_{1g} mode [34,40,41] as a result of the insusceptibility of its equilibrium position to photoexcitation, as schematically illustrated in Fig. 1(c). The anisotropic optical polarization dependence confirmed the generation of the E_g phonon is dominated by the impulsive stimulated Raman scattering (ISRS) mechanism at low excitation densities [19]. With a sufficiently short light field and a short-lived intermediate state (impulsive limit) the ionic displacement can be expressed as [30,42,43]

$$Q_y(t) = Q_y^0 \exp(-\Gamma_y t) \sin(2\pi \nu_y t). \quad (2)$$

A DFT study [13] predicted strong coupling between the E_g and A_{1g} modes under intense photoexcitation. The coupling was experimentally demonstrated by the emergence of a combination mode at the difference frequency in a prior TR study [44]. The literature also reported a coherent E_g amplitude as a function of pump fluence based on its fast Fourier transform (FFT) peak height obtained from the standard (isotropic) TR detection. The FFT spectra featured a much larger A_{1g} peak as well, however; at high fluences the asymmetrically broadened A_{1g} peak overlapped and obscured the E_g peak, which left considerable uncertainty in the quantitative evaluation of the latter mode.

In the present study we experimentally investigate coherent E_g phonons in Bi under intense photoexcitation by employing an anisotropic detection scheme in which the isotropic A_{1g} contribution to the TR signals could, in principle, be canceled. To maximize the E_g phonon signal we choose a bulk single-crystal Bi whose crystalline axes are well specified and keep it at a low temperature of 11 K [19,44]. For comparison we also examine the fluence dependences of the A_{1g} mode and photoexcited carriers in the standard (isotropic) detection scheme. We find that the amplitudes of the two phonon modes exhibit strikingly different fluence dependences and interpret the re-

sults in the context of dynamic coupling of the E_g phonons with the A_{1g} mode and with nonequilibrium photocarriers. On the other hand, the initial phases of the two coherent phonons shift in parallel with increasing fluence, suggesting a fluence-dependent transition time from the ground state to the excited state.

II. EXPERIMENT

The sample studied is a 1-mm-thick bulk single-crystal Bi with a (0001)-oriented polished surface in hexagonal notation [or (111) in cubic notation], which was purchased from MaTeck and was used without further treatment. The crystal was mounted in a closed-cycle cryostat with its $[11\bar{2}0]$ axis in the vertical direction and was kept at 11 K.

Single-color pump-probe reflectivity measurements were performed on the Bi crystal with an output of a regenerative amplifier with 120-fs duration, 810-nm center wavelength (1.53-eV photon energy), and 100-kHz repetition rate as the light source. An $f = 100$ mm plano-convex lens focuses the linearly polarized pump and probe beams to the ~ 80 - and 40 - μm spots on the sample with incident angles of $< 5^\circ$ and 15° from the surface normal, respectively. Incident pump fluence was adjusted between $F_{\text{inc}} = 0.40$ and 28 mJ/cm^2 by rotating a half-wave plate before a fixed plate-type polarizer located in front of the focusing lens. The pump beam was modulated with an optical chopper for lock-in detection.

To examine the E_g phonons we measured anisotropic transient reflectivity, $\Delta R_{eo} \equiv \Delta R_H - \Delta R_V$, by employing the incident probe polarized at $\sim 45^\circ$ from horizontal (H) and by detecting the H and vertical (V) polarization components of the reflected probe light with a pair of matched photodiode detectors. For comparison we also measured electronic and A_{1g} responses in the standard (isotropic) TR scheme, in which the pump-induced change in reflectivity ΔR is measured by detecting the probe light before and after reflection at the sample surface with a pair of matched photodetectors. In both detection configurations, the signal from the detector pair was amplified with a current preamplifier and a lock-in amplifier. Time delay t between the pump and probe pulses was scanned step by step with a translational stage (slow scan).

For a Bi crystal with *moderate* coherent ionic displacements Q_i , photoexcited carrier density N , and lattice temperature T_l , the standard TR signal can be approximately expressed by:

$$\frac{\Delta R(t)}{R} = \frac{1}{R} \left[\sum_i \left(\frac{\partial R}{\partial Q_i} \right) Q_i(t) + \left(\frac{\partial R}{\partial N} \right) N(t) + \left(\frac{\partial R}{\partial T_l} \right) \Delta T_l(t) \right], \quad (3)$$

with $i = y$ and z denoting the displacements along the E_g and A_{1g} coordinates. In the anisotropic detection scheme the last two terms of Eq. (3) and the A_{1g} contribution to the first term are canceled since they are isotropic within the surface plane. The scheme therefore enables us to monitor the E_g phonon response exclusively:

$$\frac{\Delta R_{eo}(t)}{R} = \frac{1}{R} \left(\frac{\partial R}{\partial Q_y} \right) Q_y(t). \quad (4)$$

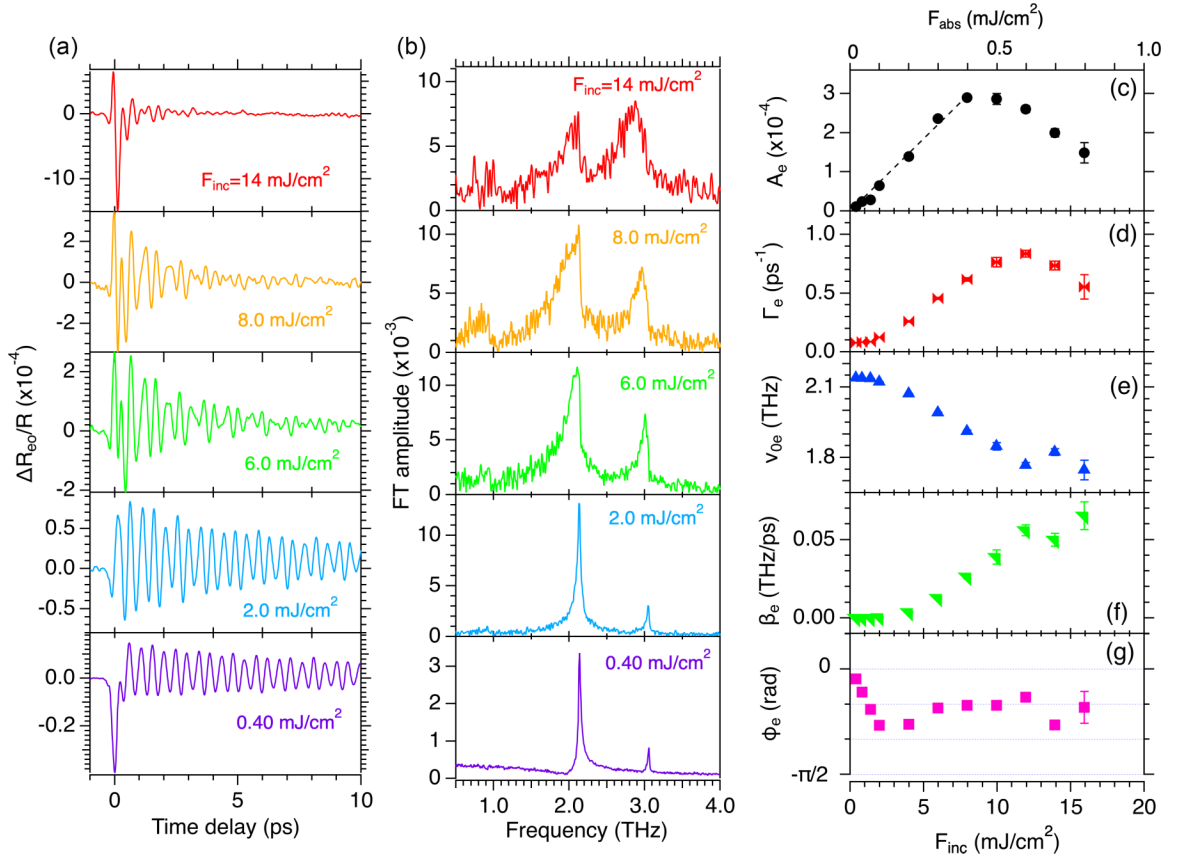


FIG. 2. (a) Anisotropic TR signals of the Bi(0001) surface obtained at 11 K with different pump fluences. Pump light is polarized parallel to the [11 $\bar{2}$ 0] axis. (b) Fast Fourier transform (FFT) spectra of the oscillatory part of (a). (c) to (g) Pump fluence dependences of (c) the amplitude, (d) dephasing rate, (e) initial frequency, (f) frequency chirp, and (g) initial phase of the coherent E_g phonon obtained by fitting the reflectivity signals in (a) to Eq. (5). The dashed line in (c) indicates a linear fit in the low-fluence regime.

For a crystal far from equilibrium under extremely intense photoexcitation, however, Eqs. (3) and (4) may no longer be adequate because of the contributions of the higher-order terms and/or because the crystal may be approaching a photoinduced phase transition [45,46].

III. RESULTS

A. Coherent E_g phonon

We first examine the E_g phonon dynamics in the anisotropic detection scheme. Figure 2(a) shows the anisotropic TR signals ΔR_{eo} at selected incident fluences F_{inc} . Here the pump polarization is set to be parallel to the [11 $\bar{2}$ 0] crystalline axis to maximize the E_g phonon contribution, and the probe is polarized at $\sim 45^\circ$ to it for anisotropic detection [19]. At the minimum fluence of $F_{inc} = 0.40$ mJ/cm² the TR signal shows a negative spike at $t = 0$, followed by a periodic modulation predominantly due to the E_g phonon at ~ 2 THz. The FFT spectrum in Fig. 2(b) shows a small A_{1g} peak at 3 THz as well, however, due to the imperfect optical polarization in the experiments. As the fluence is increased, the E_g peak is broadened and redshifted, in agreement with prior TR studies [40,44]. Meanwhile, the A_{1g} peak grows with fluence and eventually becomes higher than the E_g peak. At $F_{inc} = 16$ mJ/cm² the baseline of the signal exhibits large fluctuation, as shown in Fig. S1(a) in the Supplemental Material (SM)

[30]. We check the reversibility of the fluence dependence by measuring the same spot again at a low fluence; these results are summarized in Figs. S1(b) and S1(c) in the SM [30]. We find that the signal after exposure to the maximum fluence is as noiseless as that from a fresh spot. The E_g amplitudes before and after the exposure are comparable, and so are the dephasing rates (the linewidths). These results indicate that no significant irreversible damage such as melting was induced by the exposure.

To quantitatively analyze the fluence dependence of the coherent E_g phonons we fit the oscillatory component of the time-domain TR signals to the sum of two damped harmonic functions:

$$\frac{\Delta R_{osc}}{R} = A_e \exp(-\Gamma_e t) \sin[2\pi \nu_e t + \phi_e] + A_a \exp(-\Gamma_a t) \sin[2\pi \nu_a t + \phi_a], \quad (5)$$

where the subscripts e and a denote the E_g and A_{1g} modes. For simplicity we assume linear chirps in the frequencies:

$$\nu_i = \nu_{0i} + \beta_i t, \quad (6)$$

with i denoting e or a . This function can give excellent fits to the TR signals for $t > 0.3$ ps, as demonstrated in Fig. S3 in the SM [30], whereas for $t < 0.3$ ps the fitting is somewhat poorer because of the large negative spike overlapping around $t = 0$. Figures 2(c)–2(g) summarize the E_g phonon parameters

obtained by the fitting as a function of incident pump fluence. The initial frequency ν_{0e} redshifts from 2.1 to 1.8 THz, and the linear chirp β_e increases from $<10^{-4}$ to 0.06 THz/ps, whereas the dephasing rate Γ_e increases from 0.08 to 0.8 ps $^{-1}$, with increasing fluence from 0.40 to 12 mJ/cm 2 .

Surprisingly, the E_g amplitude is found to increase almost linearly only up to $F_{\text{inc}} \simeq 8$ mJ/cm 2 and then to turn to an apparent decrease [Fig. 2(c)]. The decrease is *not* due to irreversible photoinduced damage since the fluence dependence is reversible, as we see in Fig. S1 in the SM [30]. We also confirm that the behavior is independent of the analysis method; the area under the E_g peak in the FFT spectra similarly increases and then decreases with fluence, as shown in Fig. S4 in the SM [30]. We note that a previous TR study [44] reported a fluence dependence of the E_g amplitude that appeared to contradict the present result. This is because that study estimated the E_g amplitude as the FFT peak height from the standard (isotropic) TR signals. In this case the E_g peak height can be overestimated considerably due to the overlapping A_{1g} peak, as we also reproduced in the standard TR experiments shown in Fig. S5 of the SM [30].

The initial phase of the E_g phonon [Fig. 2(g)] is found to be close to a sine function of time ($\phi_e = 0$) at the minimum fluence, as is expected for an excitation in the impulsive limit [Eq. (2)] with a δ -function-like driving force. With increasing fluence the phase first steeply decreases to $\phi_e \sim -\pi/4$ and then recovers partially to $\phi_e \sim -\pi/6$. The deviation of the initial phase from zero indicates that the duration of the driving force can no longer be negligible compared to the phonon period. We note that in the low-fluence regime ($F_{\text{inc}} < 6$ mJ/cm 2), where we observe the most prominent phase shift, the fitting results are excellent (see Fig. S3 in the SM [30]), which ensures reliable determination of the phase. In the high-fluence regime ($F_{\text{inc}} > 6$ mJ/cm 2) the fit has somewhat larger uncertainty, however, due to the faster dephasing of the E_g oscillation as well as the larger contributions from the negative spike at $t = 0$. The poorer fitting may be the cause for the larger scatter in the initial phase in the high-fluence regime. We also perform similar anisotropic TR measurements using longer pump pulses, the results of which are summarized in Fig. S6 in the SM [30]. We find ϕ_e to exhibit a qualitatively similar, if less pronounced, shift with fluence for a longer pulse duration, confirming that the phase shift is no artifact of the experiments.

B. Electronic and thermal responses

To examine the origin of the unconventional fluence dependence of the E_g phonon we also examine the carrier and A_{1g} phonon dynamics of the Bi crystal sample excited under the same conditions in the standard TR detection scheme. The pump and probe light polarizations are set at 45 $^\circ$ and 0 $^\circ$ to the [1120] axis, respectively, to minimize the E_g contribution to the signals [19]. The standard TR signals, shown in Fig. 3(a), feature a sizable nonoscillatory response of photoexcited carriers in addition to the oscillatory coherent phonon response. The former can be fitted to a multiexponential function on top

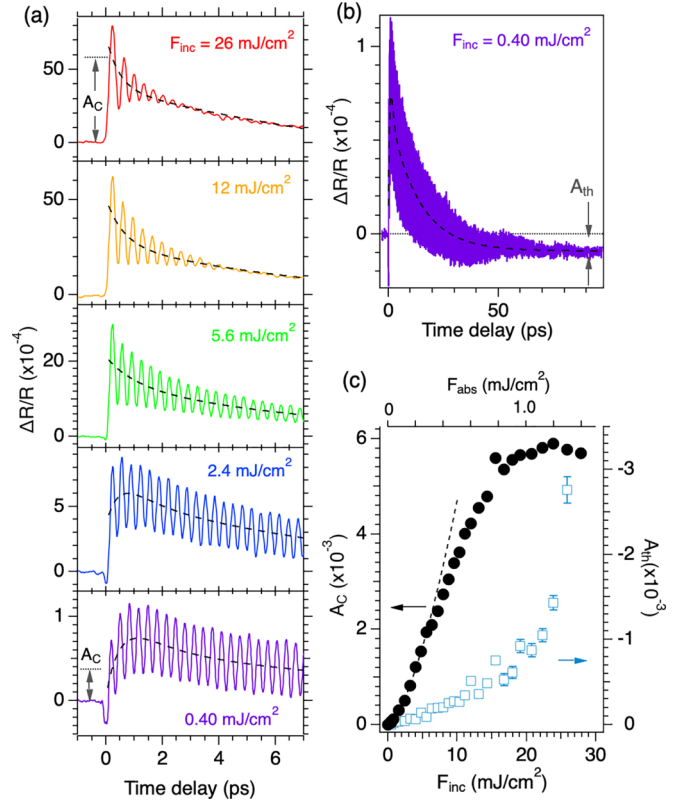


FIG. 3. (a) and (b) Standard TR signals of Bi (solid curves) obtained at 11 K for different pump fluences. Dashed curves represent the nonoscillatory response obtained by fitting to Eq. (7). (c) Height of the nonoscillatory response at $t = 0.2$ ps (A_c , filled circles, plotted on the left axis) and the baseline at a long time delay (A_{th} , open squares, on the right axis) as a function of pump fluence. The dashed curve represents the extrapolation of the fitting to a power function ($A_c \propto F_{\text{inc}}^n$) in the low-fluence regime ($F_{\text{inc}} < 6$ mJ/cm 2).

of a baseline,

$$\frac{\Delta R_{\text{non}}}{R} = \sum_j A_j \exp(-t/\tau_j) + A_{th}, \quad (7)$$

whose results are indicated by the dashed curves in Figs. 3(a) and 3(b).

At the lowest fluence examined ($F_{\text{inc}} = 0.40$ mJ/cm 2) the nonoscillatory component can be fitted reasonably to the sum of an exponential function for the rise and two for the decay. The obtained rise time, $\tau_{\text{rise}} = 0.6$ ps, is in agreement with that reported for the intervalley electron-phonon scatterings [47,48]. The decay time constants are found to be $\tau_{\text{fast}} = 0.9$ ps and $\tau_{\text{slow}} = 13$ ps; the latter is slower than the time constants of the energy dissipation to the lattice (4 ps) and of the electron-hole recombination (2.5 ps) reported in previous studies [47,49], possibly because of the lower temperature employed in the present study. At long time delays ($t > 30$ ps) the nonoscillatory component approaches a negative baseline A_{th} , as shown in Fig. 3(b). The value of A_{th} can be used to estimate the lattice temperature rise ΔT_l at the long time delays by adopting the temperature dependence of the reflectivity [50]:

$$\partial(\Delta R/R)/\partial T = -8 \times 10^{-5} \text{ K}^{-1}. \quad (8)$$

We would obtain $\Delta T_l < 1$ K at the minimum fluence.

With increasing fluence the initial rise in the TR signal becomes faster in time, plausibly due to larger contribution from the intraband scatterings among highly excited electrons and holes. At $F_{\text{inc}} > 4 \text{ mJ/cm}^2$ the rise is complete before the first maximum of the coherent oscillation ($\tau_{\text{rise}} \ll 0.2 \text{ ps}$) and can no longer be fitted uniquely to an exponential function. We therefore fit only the decay ($t > 0.1 \text{ ps}$) to two exponentials. In the following analyses we assume that the electrons and holes come to follow the Fermi-Dirac distribution before the first maximum of the oscillation at $t \simeq 0.2 \text{ ps}$ and regard the nonoscillatory amplitude

$$A_C \equiv \frac{\Delta R_{\text{non}}(t = 0.2 \text{ ps})}{R} \quad (9)$$

as a semiquantitative measure for photoexcited carrier density N , although the assumption of ultrafast thermalization may not hold at extremely high densities. We find that A_C grows first superlinearly ($A_C \propto F_{\text{inc}}^n$, with $n = 1.5$) up to $F_{\text{inc}} \simeq 6 \text{ mJ/cm}^2$ [dashed curve in Fig. 3(c)], then turns to a linear increase until A_C reaches a saturation at $\sim 20 \text{ mJ/cm}^2$, as shown by the filled circles in Fig. 3(c). A further increase in the fluence eventually leads to the emergence of large noise in the TR signal at $F_{\text{inc}} = 28 \text{ mJ/cm}^2$, as shown in Fig. S2 in the SM [30]. When the fluence is reduced after the exposure to the maximum fluence, we obtain a noiseless TR signal with distinct coherent phonon oscillation again, which excludes photoinduced melting and amorphization of the crystal by the exposure.

The saturation of A_C at $F_{\text{inc}} \geq 20 \text{ mJ/cm}^2$ may be interpreted as the saturation of linear optical absorption. To assess the possibility we estimate the carrier density as follows. At $t = 0$ the photoexcited carrier density N should have a depth distribution described by an exponential function of the distance from the surface x : $N(t = 0, x) = N_0 \exp(-\alpha x)$. A recent TR study on thin ($\ll 1 \mu\text{m}$) Bi films on Si substrates reported that the depth distribution becomes homogenized within 150 fs and its density at the surface reduces to 1/3–1/5 depending on the film thickness [26]. Such ultrafast homogenization of photocarriers is less likely in our bulk crystal, and for simplicity we assume the incident pump light with photon energy $\hbar\omega = 1.53 \text{ eV}$ is absorbed uniformly and completely within the optical penetration depth $1/\alpha = 14.7 \text{ nm}$:

$$N(t \simeq 0) = \begin{cases} (1 - R)F_{\text{inc}}\alpha/(\hbar\omega) & \text{for } 0 < x < 1/\alpha, \\ 0 & \text{for } x > 1/\alpha, \end{cases} \quad (10)$$

which will give an upper limit of the carrier density at the surface. As for the reflectivity at 11 K we tentatively estimate $R = 0.95$ by extrapolating the reflectivity reported for higher temperatures [36,51], as discussed in Fig. S7 in the SM [30]. The absorbed fluence $F_{\text{abs}} \equiv (1 - R)F_{\text{inc}}$ obtained by using this reflectivity value is plotted on the top axes of Figs. 2(c)–2(g), 3(c), and 4(b)–4(f). This choice is justified by the quantitative agreement of the fluence dependence of the A_{1g} frequency, shown in Fig. S9 in the SM [30], with that reported for a 197-nm-thick Bi film at room temperature [26]. At $F_{\text{inc}} = 20 \text{ mJ/cm}^2$, at which A_C reaches saturation, we would obtain $N = 2.8 \times 10^{21} \text{ cm}^{-3}$. This density would

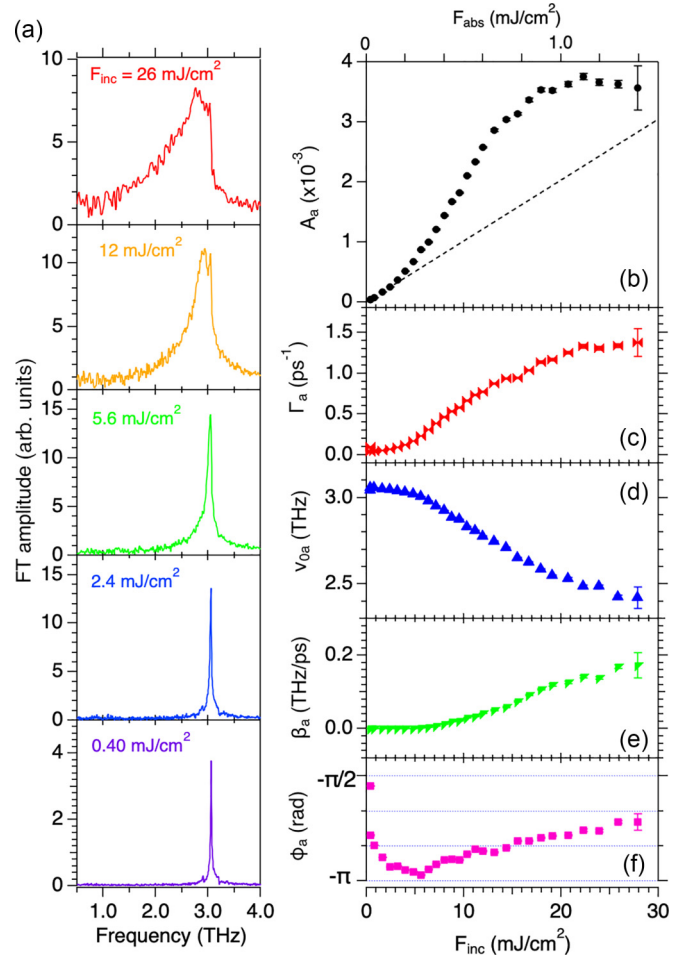


FIG. 4. (a) FFT spectra of the oscillatory part of TR signals shown in Fig. 3(a). (b) to (f) Fluence dependences of (b) the amplitude, (c) dephasing rate, (d) initial frequency, (e) frequency chirp, and (f) initial phase of the coherent A_{1g} phonon, obtained by fitting the oscillatory reflectivity signals to the second term in Eq. (5). The dashed line in (b) represents the extrapolation of a linear fitting in the low-fluence regime ($F_{\text{inc}} < 3 \text{ mJ/cm}^2$).

correspond to 2% of the valence electrons of Bi:

$$N_v = 5N_A w/M = 1.4 \times 10^{23} \text{ cm}^{-3}, \quad (11)$$

with 5 being the number of valence electrons per Bi atom, N_A being the Avogadro constant, $w = 9.747 \text{ g/cm}^3$ being the density of Bi, and $M = 209$ being the atomic number. It would be reasonable to expect the linear absorption to be saturated at such a high carrier density.

At long time delays ($t \gg 10 \text{ ps}$) we obtain the baseline A_{th} by fitting the TR signals to Eq. (7) and estimate the equilibrium lattice temperature using Eq. (8). A_{th} increases almost linearly with fluence up to $F_{\text{inc}} = 20 \text{ mJ/cm}^2$ and then turns to a steeper increase, as plotted by the open symbols in Fig. 3(c). At the maximum fluence examined, the lattice temperature rise is estimated to be $\Delta T_l \simeq 35 \text{ K}$.

C. Coherent A_{1g} phonon

The A_{1g} phonon response can be extracted from the TR signals in Fig. 3(a) by subtracting the nonoscillatory component

(dashed curves). The FFT spectra shown in Fig. 4(a) feature only the A_{1g} peak at 3 THz, confirming that the E_g contribution is minimized with the selected pump and probe light polarizations. We accordingly fit the oscillatory signals to only the second term of Eq. (5), either over the entire time range or over the first three cycles of the oscillations, as was done in some of the previous studies. The results of the two fittings are compared in Figs. S8 and S9 in the SM [30]. Although neither reproduces the experimental oscillations perfectly at all the pump fluences, the A_{1g} phonon parameters obtained from the two fittings are in reasonable agreement. We therefore discuss only the phonon parameters obtained from the fitting over the entire time window, which are summarized in Figs. 4(b)–4(f).

The A_{1g} amplitude increases linearly in the low-fluence regime ($F_{\text{inc}} < 3 \text{ mJ/cm}^2$), as indicated with a dashed line in Fig. 4(b), but grows superlinearly ($A_a \propto F_{\text{inc}}^{1.5}$) in the intermediate-fluence regime ($F_{\text{inc}} = 3\text{--}15 \text{ mJ/cm}^2$). A further increase in the fluence leads to saturation of the amplitude in the high-fluence regime ($F_{\text{inc}} > 20 \text{ mJ/cm}^2$) and eventually to the emergence of large noise in the TR signal during the time delay scan, as we have already seen in Fig. S2(a) in the SM [30]. When the fluence is reduced after exposure to the maximum fluence, we obtain coherent A_{1g} oscillation whose initial amplitude is almost as large as that before the exposure, but the dephasing is faster, as shown in Figs. S2(b) and S2(c). The comparison indicates a small irreversible change in the crystal, such as slight damage at the surface, but no sign of complete melting or other phase transition.

The observed fluence dependence of the A_{1g} amplitude is in quantitative agreement with a prior TR study performed under similar conditions (on a 1-mm-thick Bi single crystal at 5 K) [52]. The behavior is also in rough, although not perfect, agreement with that of the electronic response A_C [filled circles in Fig. 3(c)], suggesting that the saturation of the A_{1g} amplitude has the same origin as that of A_C . On the other hand, it is in striking contrast to the fluence dependences of the E_g amplitude [Fig. 2(c)], which starts to decrease already at $F_{\text{inc}} \simeq 10 \text{ mJ/cm}^2$, while the A_{1g} amplitude still grows superlinearly. The contrast *excludes* the possibility that the E_g amplitude decreases because the entire crystalline lattice is becoming unstable by approaching the high-symmetry phase, for example.

The initial phase ϕ_a is close to a cosine function of time ($\phi_a = -\pi/2$) at the minimum fluence of $F_{\text{inc}} = 0.4 \text{ mJ/cm}^2$, as expected for coherent phonons excited in the displacive limit [Eq. (1)] with a Heaviside-step-function-like driving force. With increasing fluence the initial phase first shifts steeply down to $\phi_a \simeq -\pi$ and then gradually recovers to $\phi_a = -2\pi/3$. We note that fitting results are excellent throughout the entire fluence range examined, as shown in Fig. S8 in the SM [30], ensuring reliable determination of the initial phase. We also observe a consistent phase shift with fluence in the standard TR measurements using longer pump pulses, as shown in Fig. S6(b) in the SM [30]. On the one hand, in the DECP model the initial phase can deviate from a cosine function if the driving force is not a Heaviside step function but has a finite decay time [15]. On the other hand, we notice that the initial phase of the E_g phonon [Fig. 2(g)] also shifts with fluence, almost in parallel to that of A_{1g} . The parallel trends of the two modes could be better explained by a finite *rise* time in the driving forces, which could affect both

the Heaviside-step-function-like and δ -function-like driving forces for the A_{1g} and E_g modes.

The rise in carrier-phonon coupling after photoexcitation may be visualized by performing a time-windowed Fourier transform on the whole TR signal containing both the electronic and phononic responses [colored curves in Fig. 3(a)]. The results obtained with a Gaussian time window of half width $\Delta t = 0.33 \text{ ps}$, which allows us the best balance between the temporal and frequency resolutions ($\Delta\nu \simeq 0.5 \text{ THz}$), are presented as false-color plots in Fig. 5. At the lowest fluence [Fig. 5(a)] the phononic response at $\sim 3 \text{ THz}$ and the electronic response at $\lesssim 1 \text{ THz}$ are well separated from each other; they both emerge within the time window width used in the analysis. With increasing fluence the electronic response acquires a higher-frequency component at early time delays, which interconnects it with the phononic response in the first fraction of a picosecond. At later time delays the coupled electron-phonon response (solid curves in Fig. 5) approaches the intrinsic A_{1g} phonon frequency (dash-dotted curves in Fig. 5). The timescale for this transient blueshift is comparable to the time window width at the minimum fluence ($F_{\text{inc}} = 0.4 \text{ mJ/cm}^2$) but becomes as slow as $\gtrsim 1 \text{ ps}$ at the maximum fluence. This observation may be interpreted in terms of the fluence-dependent transition time from the ground-state PES to the excited-state PES, as was predicted for the A_1 phonon of tellurium, another elemental semimetal with Peierls instability, by recent time-dependent DFT simulations [53]. We note that there is a notable discrepancy between the transient blueshift obtained from the time-windowed analyses (solid lines in Fig. 5) and that estimated from the time-domain fitting to Eq. (5) (dashed lines). The discrepancy can be regarded as the manifestation of the excited-state PES still shifting and deforming towards a new equilibrium. The two frequencies eventually coincide after the system reaches the equilibrium in the low- and intermediate-fluence regimes. In the high-fluence regime ($F_{\text{inc}} > 15 \text{ mJ/cm}^2$), however, the two frequencies no longer coincide on reasonable timescale, implying the failure of assuming a linear frequency chirp in this regime.

IV. DISCUSSION

We now discuss the origin of the unconventional fluence dependence of the E_g phonon amplitude [Fig. 2(c)], which is in stark contrast to the behavior of the A_{1g} amplitude [Fig. 4(b)].

A prior DFT study [13] calculated excited-state PESs as a function of the E_g and A_{1g} coordinates. Figures 6(a) and 6(b) partially reconstruct the reported two-dimensional (2D) PESs around the ground-state equilibrium ($z = Q_z^{\text{min}} = 0.234$ and $y = 0$) for two selected densities of photoexcited electron-hole pairs N_{e-h} . The 2D PESs over the entire calculated displacements, showing the double-well potential along the A_{1g} coordinate, are reconstructed in Fig. S10(a) in the SM [30] for all four densities reported in the literature. Upon photoexcitation the equilibrium shifts along the z coordinate from Q_z^{min} to $Q_z^E(N_{e-h})$. This gives a driving force to Bi ions to oscillate between the ground-state equilibrium Q_z^{min} and the maximum $Q_z^{\text{max}} = 2Q_z^E - Q_z^{\text{min}}$ via the DECP mechanism. In the y coordinate the ions oscillate around $y = 0$ via the ISRS mechanism, whose amplitude was not obtained from the

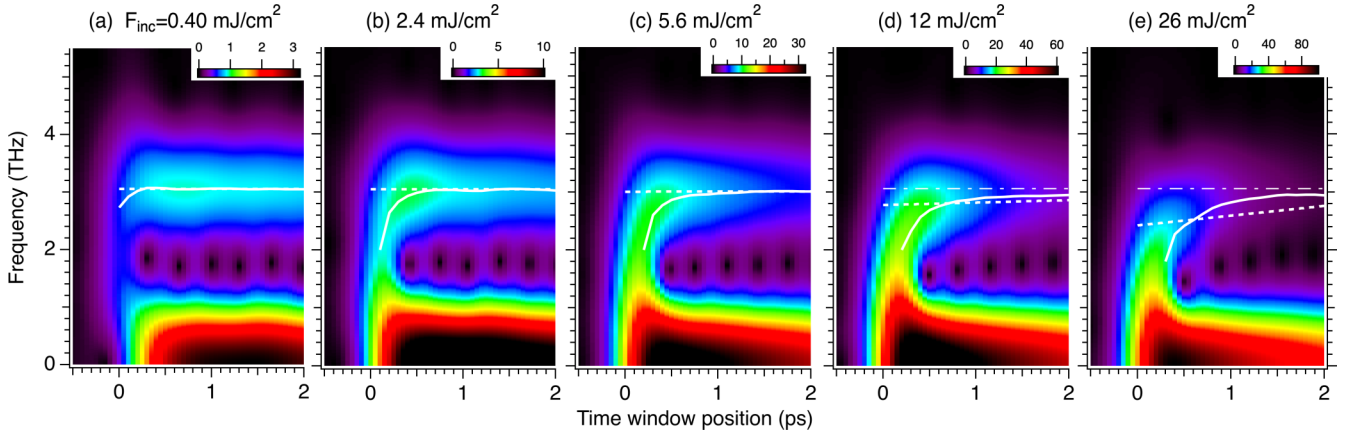


FIG. 5. False-color plots of the time-windowed FFT amplitude of the TR signals in Fig. 3(a) as functions of time window position and frequency. A Gaussian time window of 330-fs half width at half maximum is used. Solid curves represent the peak positions within the frequency range of 2–3.5 THz. Dashed lines reproduce the linearly chirped A_{1g} frequency $\nu_a = \nu_{a0} + \beta_a t$ using parameters plotted in Figs. 4(d) and 4(e). Dashed-dotted lines represent the intrinsic A_{1g} frequency.

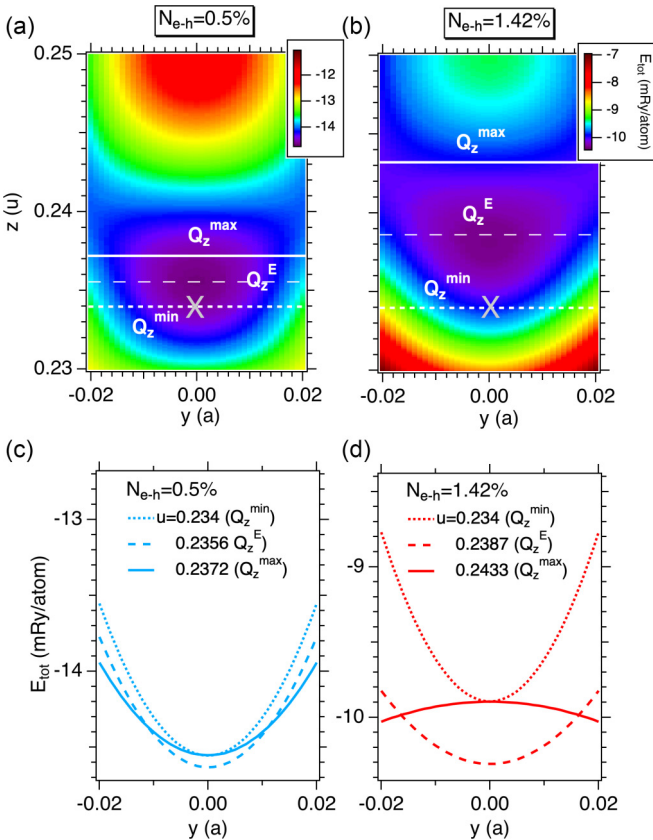


FIG. 6. (a) and (b) Excited-state PESs at photoexcitation of (a) 0.5% and (b) 1.42% of valence electrons, as reproduced by using the parameters obtained by DFT simulations in Ref. [13]. y and z represent the E_g and A_{1g} coordinates in units of the hexagonal lattice constant a and in the form of the internal displacement parameter u , respectively. Crosses represent the ground-state minimum at $z = Q_z^{\min} = 0.234$ and $y = 0$. Dashed and solid lines denote the equilibrium on the excited state Q_z^E and the maximum displacement Q_z^{\max} in the A_{1g} coordinate. (c) and (d) Slices of the two-dimensional PES along the E_g coordinate for different values of u at photoexcitation of (c) 0.5% and (d) 1.42% of valence electrons.

calculations but was estimated to be an order of magnitude smaller than A_{1g} in a previous trXRD study [34].

At a low excitation density, where the displacements are small and the PES can be approximated to be harmonic, one could assume that the E_g and A_{1g} oscillations are independent of each other. Even in the case of $N_{e-h} = 0.5\%$ of valence electrons, however, the PES slice along the y coordinate, shown in Fig. 6(c), is not perfectly independent of the A_{1g} displacement and experiences a small disturbance as a function of z . With increasing N_{e-h} the maximum Q_z^{\max} , indicated by the solid lines in Figs. 6(a) and 6(b), approaches the central barrier at $z = 0.25$, while the barrier becomes lower. This introduces significant deformation in the PES slice along the y coordinate as z varies from Q_z^{\min} to Q_z^{\max} , i.e., within a half cycle of the A_{1g} oscillation. At $N_{e-h} = 1.42\%$, the PES along the y coordinate suffers such significant deformation that the curvature of the PES slice becomes negative when the ion reaches Q_z^{\max} , as shown in Fig. 6(d). We infer that this deformation of the PES will lead to a quick loss of the vibrational coherence of the E_g mode within a single cycle of the A_{1g} oscillation and thereby to an effective suppression of coherent E_g phonons at high fluences, as observed in Fig. 2.

A further increase in the excitation density above 2% would transform the double-well PES in the z coordinate to a single well, as illustrated in Fig. 1(c), according to another DFT simulation [12]. A single-shot TR study [38] reported a gradual decrease in the A_{1g} oscillation amplitude with increasing fluence and complete disappearance at $F_{\text{inc}} > 10 \text{ mJ/cm}^2$ ($F_{\text{abs}} > 3 \text{ mJ/cm}^2$) for a 275-nm-thick Bi film at room temperature. The disappearance was interpreted as the result of a photoinduced transition to the theoretically predicted high-symmetry phase. A trXRD study on a 50-nm-thick Bi film at room temperature reported a similar disappearance of the oscillation at $F_{\text{abs}} > 3 \text{ mJ/cm}^2$ [54]. In the present study, which we believe stayed below the reported threshold fluence, we did not observe such complete disappearance of the A_{1g} oscillation. Instead, we observed large noise in the TR signal to appear halfway through the scan of the time delay (Fig. S2 in the SM [30]), which is indicative of partial damage of the

crystal surface as a result of continuous heating due to the repetitive excitation at 100 kHz at a high fluence. We speculate that the lattice cooling at the surface of our 1-mm-thick Bi crystal could be less efficient than in a sub-micron-thick film on a substrate due to the low thermal conductivity of Bi [55].

V. CONCLUSION

The ultrafast dynamics of coherent E_g phonons of bulk single-crystal Bi was investigated under intense photoexcitation at low temperature. With increasing pump fluence the E_g amplitude reached its maximum and started to decrease at a significantly lower fluence than the A_{1g} amplitude became saturated. These contrasting behaviors were explained

in terms of the strong coupling of the E_g oscillation with the large-amplitude A_{1g} oscillation on the highly excited electronic state, which could lead to suppression of the former oscillation via dynamic deformation of the PES. By contrast, the fluence dependence of the A_{1g} phonons is dominated by the coupling with photoexcited carriers rather than that with the E_g phonon. The phase shifts of the two phonon modes with fluence could be an indication of a carrier density-dependent transition time from the ground-state PES to the excited-state one.

ACKNOWLEDGMENT

K.I. thanks Dr. Y. Kubota and Dr. Y. Shinohara for their valuable discussions.

-
- [1] A. B. Shick, J. B. Ketterson, D. L. Novikov, and A. J. Freeman, Electronic structure, phase stability, and semimetal-semiconductor transitions in Bi, *Phys. Rev. B* **60**, 15484 (1999).
- [2] Y. Ohtsubo, L. Perfetti, M. O. Goerbig, P. L. Fevre, F. Bertran, and A. Taleb-Ibrahimi, Non-trivial surface-band dispersion on Bi(111), *New J. Phys.* **15**, 033041 (2013).
- [3] I. Aguilera, C. Friedrich, and S. Blügel, Electronic phase transitions of bismuth under strain from relativistic self-consistent GW calculations, *Phys. Rev. B* **91**, 125129 (2015).
- [4] F. Schindler, Z. Wang, M. G. Vergniory, A. M. Cook, A. Murani, S. Sengupta, A. Y. Kasumov, R. Deblock, S. Jeon, I. Drozdov, H. Bouchiat, S. Gueron, A. Yazdani, B. A. Bernevig, and T. Neupert, Higher-order topology in bismuth, *Nat. Phys.* **14**, 918 (2018).
- [5] A. K. Nayak, J. Reiner, R. Queiroz, H. Fu, C. Shekhar, B. Yan, C. Felser, N. Avraham, and H. Beidenkopf, Resolving the topological classification of bismuth with topological defects, *Sci. Adv.* **5**, eaax6996 (2019).
- [6] K.-H. Jin, H. W. Yeom, and F. Liu, Doping-induced topological phase transition in Bi: The role of quantum electronic stress, *Phys. Rev. B* **101**, 035111 (2020).
- [7] C. Y. Wu, J. C. Han, L. Sun, H. R. Gong, and C. P. Liang, Effects of trigonal deformation on electronic structure and thermoelectric properties of bismuth, *J. Phys.: Condens. Matter* **30**, 285504 (2018).
- [8] C. Y. Wu, L. Sun, H. R. Gong, and S. F. Zhou, Influence of internal displacement on band structure, phase transition, and thermoelectric properties of bismuth, *J. Mater. Sci.* **54**, 6347 (2019).
- [9] M. Zouhar and M. Sob, *Ab initio* study of deformed As, Sb, and Bi with an application to thin films, *Phys. Rev. B* **94**, 184110 (2016).
- [10] N. P. Armitage, R. Tediosi, F. Levy, E. Giannini, L. Forro, and D. van der Marel, Infrared conductivity of elemental bismuth under pressure: Evidence for an avoided Lifshitz-type semimetal-semiconductor transition, *Phys. Rev. Lett.* **104**, 237401 (2010).
- [11] P. Brown, K. Semeniuk, A. Vasiljkovic, and F. M. Grosche, Pressure-induced semimetal-to-semiconductor transition in bismuth, *Phys. Procedia* **75**, 29 (2015).
- [12] E. D. Murray, D. M. Fritz, J. K. Wahlstrand, S. Fahy, and D. A. Reis, Effect of lattice anharmonicity on high-amplitude phonon dynamics in photoexcited bismuth, *Phys. Rev. B* **72**, 060301(R) (2005).
- [13] E. S. Zijlstra, L. L. Tatarinova, and M. E. Garcia, Laser-induced phonon-phonon interactions in bismuth, *Phys. Rev. B* **74**, 220301(R) (2006).
- [14] T. K. Cheng, J. Vidal, H. J. Zeiger, G. Dresselhaus, M. S. Dresselhaus, and E. P. Ippen, Mechanism for displacive excitation of coherent phonons in Sb, Bi, Te and Ti_2O_3 , *Appl. Phys. Lett.* **59**, 1923 (1991).
- [15] H. J. Zeiger, J. Vidal, T. K. Cheng, E. P. Ippen, G. Dresselhaus, and M. S. Dresselhaus, Theory for displacive excitation of coherent phonons, *Phys. Rev. B* **45**, 768 (1992).
- [16] T. Cheng, S. Brorson, A. Kazeroonian, J. Moodera, G. Dresselhaus, M. Dresselhaus, and E. P. Ippen, Impulsive excitation of coherent phonons observed in reflection in bismuth and antimony, *Appl. Phys. Lett.* **57**, 1004 (1990).
- [17] M. Hase, M. Kitajima, S. I. Nakashima, and K. Mizoguchi, Dynamics of coherent anharmonic phonons in bismuth using high density photoexcitation, *Phys. Rev. Lett.* **88**, 067401 (2002).
- [18] O. Misochko, M. Hase, K. Ishioka, and M. Kitajima, Observation of an amplitude collapse and revival of chirped coherent phonons in bismuth, *Phys. Rev. Lett.* **92**, 197401 (2004).
- [19] K. Ishioka, M. Kitajima, and O. Misochko, Temperature dependence of coherent A_{1g} and E_g phonons of bismuth, *J. Appl. Phys.* **100**, 093501 (2006).
- [20] D. Boschetto, E. G. Gamaly, A. V. Rode, B. Luther-Davies, D. Glijer, T. Garl, O. Albert, A. Rousse, and J. Etchepare, Small atomic displacements recorded in bismuth by the optical reflectivity of femtosecond laser-pulse excitations, *Phys. Rev. Lett.* **100**, 027404 (2008).
- [21] H. Katsuki, J. C. Delagnes, K. Hosaka, K. Ishioka, H. Chiba, E. S. Zijlstra, M. E. Garcia, H. Takahashi, K. Watanabe, M. Kitajima, Y. Matsumoto, K. G. Nakamura, and K. Ohmori, All-optical control and visualization of ultrafast two-dimensional atomic motions in a single crystal of bismuth, *Nat. Commun.* **4**, 2801 (2013).
- [22] Y. M. Sheu, Y. J. Chien, C. Uher, S. Fahy, and D. A. Reis, Free-carrier relaxation and lattice heating in photoexcited bismuth, *Phys. Rev. B* **87**, 075429 (2013).
- [23] O. V. Misochko, M. V. Lebedev, and E. V. Lebedeva, Inhomogeneity as a source of collapse and revival for large-amplitude

- chirped coherent A_{1g} phonons in bismuth, *Phys. Rev. B* **90**, 014301 (2014).
- [24] Y.-H. Cheng, F. Y. Gao, S. W. Teitelbaum, and K. A. Nelson, Coherent control of optical phonons in bismuth, *Phys. Rev. B* **96**, 134302 (2017).
- [25] R. Geneaux, I. Timrov, C. J. Kaplan, A. D. Ross, P. M. Kraus, and S. R. Leone, Coherent energy exchange between carriers and phonons in Peierls-distorted bismuth unveiled by broadband xuv pulses, *Phys. Rev. Res.* **3**, 033210 (2021).
- [26] F. Thiemann, G. Sciaini, A. Kassen, U. Hagemann, F. Meyer zu Heringdorf, and M. Horn-von Hoegen, Ultrafast transport-mediated homogenization of photoexcited electrons governs the softening of the A_{1g} phonon in bismuth, *Phys. Rev. B* **106**, 014315 (2022).
- [27] E. Papalazarou, J. Faure, J. Mauchain, M. Marsi, A. Taleb-Ibrahimi, I. Reshetnyak, A. van Roekeghem, I. Timrov, N. Vast, B. Arnaud, and L. Perfetti, Coherent phonon coupling to individual Bloch states in photoexcited bismuth, *Phys. Rev. Lett.* **108**, 256808 (2012).
- [28] D. Leuenberger, H. Yanagisawa, S. Roth, J. H. Dil, J. W. Wells, P. Hofmann, J. Osterwalder, and M. Hengsberger, Excitation of coherent phonons in the one-dimensional Bi(114) surface, *Phys. Rev. Lett.* **110**, 136806 (2013).
- [29] L. Perfetti, J. Faure, E. Papalazarou, J. Mauchain, M. Marsi, M. O. Goerbig, A. Taleb-Ibrahimi, and Y. Ohtsubo, New aspects of electronic excitations at the bismuth surface: Topology, thermalization and coupling to coherent phonons, *J. Electron Spectrosc. Relat. Phenom.* **201**, 60 (2015).
- [30] See Supplemental Material at <http://link.aps.org/supplemental/10.1103/PhysRevB.110.094313>, which includes Refs. [56,57], for the basic theory of coherent phonon generation, additional experimental results on the reversibility of the fluence dependence and on the effect of pulse duration, detailed procedures and results for the time and frequency domain fittings, discussion of the temperature-dependent reflectivity, complete reproduction of the PES calculated by Ref. [13].
- [31] K. Sokolowski-Tinten, C. Blome, J. Blums, A. Cavalleri, C. Dietrich, A. Tarasevitch, I. Uschmann, E. Förster, M. Kammler, M. Horn-von Hoegen, and D. von der Linde, Femtosecond x-ray measurement of coherent lattice vibrations near the Lindemann stability limit, *Nature (London)* **422**, 287 (2003).
- [32] D. M. Fritz *et al.*, Ultrafast bond softening in bismuth: Mapping a solid's interatomic potential with x-rays, *Science* **315**, 633 (2007).
- [33] S. L. Johnson, P. Beaud, C. J. Milne, F. S. Krasniqi, E. S. Zijlstra, M. E. Garcia, M. Kaiser, D. Grolimund, R. Abela, and G. Ingold, Nanoscale depth-resolved coherent femtosecond motion in laser-excited bismuth, *Phys. Rev. Lett.* **100**, 155501 (2008).
- [34] S. L. Johnson, P. Beaud, E. Mohr-Vorobeva, A. Caviezel, G. Ingold, and C. J. Milne, Direct observation of non-fully-symmetric coherent optical phonons by femtosecond x-ray diffraction, *Phys. Rev. B* **87**, 054301 (2013).
- [35] S. W. Teitelbaum, T. C. Henighan, H. Liu, M. P. Jiang, D. Zhu, M. Chollet, T. Sato, E. D. Murray, S. Fahy, S. O'Mahony, T. P. Bailey, C. Uher, M. Trigo, and D. A. Reis, Measurements of nonequilibrium interatomic forces using time-domain x-ray scattering, *Phys. Rev. B* **103**, L180101 (2021).
- [36] Y. Kubota, Y. Tanaka, T. Togashi, T. Ebisu, K. Tamasaku, H. Osawa, T. Wada, O. Sugino, I. Matsuda, and M. Yabashi, Suppression of atomic displacive excitation in photo-induced A_{1g} phonon mode of bismuth unveiled by low-temperature time-resolved x-ray diffraction, *Appl. Phys. Lett.* **122**, 092201 (2023).
- [37] Y. Giret, A. Gelle, and B. Arnaud, Entropy driven atomic motion in laser-excited bismuth, *Phys. Rev. Lett.* **106**, 155503 (2011).
- [38] S. W. Teitelbaum, T. Shin, J. W. Wolfson, Y.-H. Cheng, I. J. P. Molesky, M. Kandyla, and K. A. Nelson, Real-time observation of a coherent lattice transformation into a high-symmetry phase, *Phys. Rev. X* **8**, 031081 (2018).
- [39] G. Inawali, D. Boschetto, L. M. Malard, T. F. Heinz, G. Sciaini, F. Thiemann, T. Payer, L. Kremeyer, F. J. M. zu Heringdorf, and M. Horn-von Hoegen, Hot carrier transport limits the displacive excitation of coherent phonons in bismuth, *Appl. Phys. Lett.* **119**, 091601 (2021).
- [40] O. Misochko, K. Ishioka, M. Hase, and M. Kitajima, Fano interference for large-amplitude coherent phonons in bismuth, *J. Phys.: Condens. Matter* **19**, 156227 (2007).
- [41] J. J. Li, J. Chen, D. A. Reis, S. Fahy, and R. Merlin, Optical probing of ultrafast electronic decay in Bi and Sb with slow phonons, *Phys. Rev. Lett.* **110**, 047401 (2013).
- [42] L. Dhar, J. Rogers, and K. Nelson, Time-resolved vibrational spectroscopy in the impulsive limit, *Chem. Rev.* **94**, 157 (1994).
- [43] M. Först and T. Dekorsy, Coherent phonons in bulk and low-dimensional semiconductors, in *Coherent Vibrational Dynamics*, edited by S. D. Silvestri, G. Cerullo, and G. Lanzani (CRC Press, Boca Raton, FL, 2007), pp. 130–172.
- [44] O. Misochko, K. Ishioka, M. Hase, and M. Kitajima, Fully symmetric and doubly degenerate coherent phonons in semimetals at low temperature and high excitation: Similarities and differences, *J. Phys.: Condens. Matter* **18**, 10571 (2006).
- [45] M. X. Cheng, S. Z. Zhong, N. Rivas, T. Dekker, A. A. Petruk, P. Gicala, K. Pichugin, F. C. Chen, X. Luo, Y. P. Sun, A. W. Tsen, and G. Sciaini, Photoinduced interlayer dynamics in T_d -MoTe₂: A broadband pump-probe study, *Appl. Phys. Lett.* **120**, 123102 (2022).
- [46] F. Thiemann, G. Sciaini, A. Kassen, T. S. Lott, and M. Horn-von Hoegen, Disentangling the electronic and lattice contributions to the dielectric response of photoexcited bismuth, *Phys. Rev. B* **109**, L041105 (2024).
- [47] I. Timrov, T. Kampfrath, J. Faure, N. Vast, C. R. Ast, C. Frischkorn, M. Wolf, P. Gava, and L. Perfetti, Thermalization of photoexcited carriers in bismuth investigated by time-resolved terahertz spectroscopy and *ab initio* calculations, *Phys. Rev. B* **85**, 155139 (2012).
- [48] A. A. Melnikov, O. V. Misochko, and S. V. Chekalin, Ultrafast electronic dynamics in laser-excited crystalline bismuth, *J. Appl. Phys.* **114**, 033502 (2013).
- [49] C. Bronner and P. Tegeder, Relaxation dynamics of photoexcited charge carriers at the Bi(111) surface, *Phys. Rev. B* **89**, 115105 (2014).
- [50] A. Q. Wu and X. Xu, Coupling of ultrafast laser energy to coherent phonons in bismuth, *Appl. Phys. Lett.* **90**, 251111 (2007).
- [51] M. Cardona and D. L. Greenaway, Optical properties and band structure of group IV-VI and group V materials, *Phys. Rev.* **133**, A1685 (1964).
- [52] O. V. Misochko and M. V. Lebedev, Investigation of the dependence of the coherent dynamics of a bismuth lattice on

- the crystal excitation level, *J. Exp. Theor. Phys.* **109**, 805 (2009).
- [53] H. L. Ning, O. Mehio, C. Lian, X. W. Li, E. Zoghlin, P. S. Zhou, B. Y. Cheng, S. D. Wilson, B. M. Wong, and D. V. Hsieh, Light-induced Weyl semiconductor-to-metal transition mediated by Peierls instability, *Phys. Rev. B* **106**, 205118 (2022).
- [54] W. Lu, M. Nicoul, U. Shymanovich, A. Tarasevitch, M. Kammler, M. Horn-von Hoegen, D. von der Linde, and K. Sokolowski-Tinten, Extreme phonon softening in laser-excited bismuth towards an inverse Peierls-transition, *MRS Proc.* **1230**, 305 (2009).
- [55] C. F. Gallo, B. S. Chandrasekhar, and P. H. Sutter, Transport properties of bismuth single crystals, *J. Appl. Phys.* **34**, 144 (1963).
- [56] M. Hase, K. Mizoguchi, H. Harima, S. I. Nakashima, and K. Sakai, Dynamics of coherent phonons in bismuth generated by ultrashort laser pulses, *Phys. Rev. B* **58**, 5448 (1998).
- [57] T. Garl, E. G. Gamaly, D. Boschetto, A. V. Rode, B. Luther-Davies, and A. Rousse, Birth and decay of coherent optical phonons in femtosecond-laser-excited bismuth, *Phys. Rev. B* **78**, 134302 (2008).